

Penetration and Defect Formation in High-Current Arc Welding

At high currents, the weld pool turns into a thin liquid film, causing humping, undercutting, and fingerlike penetration

BY P. F. MENDEZ AND T. W. EAGAR

ABSTRACT. An explanation for penetration and defect generation in the weld pool at high currents is proposed. In this regime, the arc pressure pushes the molten metal to the rear of the weld pool, creating a thin layer of liquid metal under the arc. Premature solidification of this thin layer initiates humping, split bead, parallel humping, tunnel porosity, and undercutting. The thin nature of the liquid layer is the cause of increased penetration at high currents. We propose a simple model to predict the onset and type of humping defect.

Introduction

Increases in welding productivity have a potential economic impact of several hundred million dollars in yearly worldwide savings. Welding productivity can be improved by increasing welding speed and current; however, this strategy is limited by the appearance of weld pool defects such as humping, split bead, parallel humping, tunnel porosity, and undercutting.

Humping, also called beading, presents a weld bead with an irregular surface contour consisting of a series of beadlike protuberances, as shown in Fig. 1. In a split bead, the weld is split into two independent parallel seams separated by an empty channel. Parallel humping is a type of split bead in which the parallel seams show humping—Fig. 2. Tunnel porosity is a defect in which an open channel, which remains unfilled with weld metal, is formed at the root—Fig. 3. Undercutting is a defect in which the weld bead has parallel grooves at the side. The bottom left image of Fig. 1 illustrates the appearance of undercutting in a cross section.

In addition to the occurrence of defects, at currents above 250 A, an unexplained sudden increase in penetration with current or velocity has been reported (Refs. 1–3). The onset of this sudden

change in penetration depends on whether the current or velocity is increasing or decreasing, resembling a hysteresis cycle, as shown in Fig. 4. Both curves in this figure correspond to gas tungsten arc welding (GTAW) of steel; the left curve shows experiments performed in partial vacuum (32 mm Hg), the right curve corresponds to experiments performed at atmospheric pressure.

The generation of humping in some cases, such as laser welding or deposition of microdroplets (Ref. 4), can be understood as the consequence of a capillary instability in a long liquid body (Ref. 5–7). The capillary instability theory states that humping will occur only when the apparent contact angle, indicated as θ in Fig. 5, is larger than 90%. In this situation, humping will occur when the weld pool is longer than a critical value L_C . Table 1 presents the expressions of L_C for different approaches based on the capillary instability theory.

However, capillary instability cannot account for humping observed in bead-on-plate GTA welds, where the apparent contact angle is close to 0 deg, and other arc welds where the weld pool is not long enough to trigger a capillary instability. The occurrence of humping in these cases is frequently associated with the large depression of the weld pool under the arc observed at high currents and velocities. Some of the literature calls this depression the "gouging region." Yamamoto, Shimada et al. (Refs. 1, 2) performed research on bead-on-plate GTAW at low

pressure and observed that at the onset of humping, the weld pool was very depressed and turned into a thin film under the arc. The same effect was observed by Savage et al. (Ref. 8) in bead-on-plate GTAW at atmospheric pressure. The presence of a gouging region at high welding currents and velocities was also reported by others, including Ishizaki (Refs. 9, 10) and Bradstreet (Ref. 5), for bead-on-plate GMAW; Demyantsevich et al. (Ref. 11), for bead-on-plate GTAW; and Matsunawa et al., for GMAW in narrow grooves.

In this work, we propose that at high currents, the occurrence of weld pool defects and the sudden increase in penetration are a consequence of the same phenomenon: a change in the configuration of the weld pool between the low-current and high-current regime. At currents above 250 A, the deep depression of the free surface starts to resemble a keyhole.

Weld Pool Geometry at High Current and Velocity

Figure 6 shows top, cross, and longitudinal views of a GTA weld produced at high current and travel speed. Figure 7 shows the corresponding schematic, with its main features identified. The most salient characteristic is the deep depression of the free surface, exhibiting a "gouging region" under the arc, a "rim" of molten metal around it, and a bulk of molten metal ("trailing region") at the rear of the weld pool.

The gouging region is a very thin layer of liquid that transports molten metal to the trailing region at the rear of the weld pool. Previous studies (Refs. 13, 14) indicate that, in this region, the dominant driving force is the aerodynamic drag of the arc and the balancing force is the viscous resistance of the molten metal. Other driving forces, such as Marangoni (thermocapillary), electromagnetic, gravity, and inertial forces play a secondary role. Characteristic magnitudes of the gouging region are its temperature jump from melt-

KEY WORDS

GTAW
GMAW
Weld Defects
Humping
Porosity
High-Current Arc Welding
Stainless Steel

P. F. MENDEZ is with Exponent, Inc., Natick, Mass. T. W. EAGAR is with Massachusetts Institute of Technology, Cambridge, Mass.

Table 1 — Capillary Instability Criteria

Criterion	Critical Length	Ref.
Bradstreet	$L_C = 2\pi R$	5
Gratzke	$L_C = 2\pi R f(\theta)$	6
Schiaffino	$f(\theta) = (1 - (\pi/2\theta)^2)^{-1/2}$	7
	$L_C = 2\pi H g(\theta)$	
	$g(\theta) = (\cos\theta(\cos\theta - 1)/\beta)^{-1/2}$ $\beta = 0.67 - 9.5 \times 10^{-3}\theta + 2.36 \times 10^{-4}\theta^2 - 4.47 \times 10^{-3}\theta^3$	

ing temperature (T_C), maximum thickness (δ_C), and maximum velocity (U_C), which can be estimated by the following equations (Ref. 13).

$$\dot{T}_C = \frac{Q_{max} \dot{\delta}_C}{k} \quad (1)$$

$$\delta_C = \left(\frac{2\mu U_{\infty} D}{\tau_{max}} \right)^{1/2} \quad (2)$$

$$\dot{U}_C = \frac{\tau_{max} \dot{\delta}}{\mu} \quad (3)$$

where \dot{T}_C , $\dot{\delta}_C$, and \dot{U}_C are the estimated values of T_C , δ_C , and U_C . The symbols μ , U_{∞} , D , Q_{max} , and τ_{max} correspond to the viscosity of the molten metal, welding speed, penetration of the gouging region (indicated in Fig. 7), maximum heat input, and aerodynamic drag from the arc respectively. Typical values for the estimations above are $\dot{T}_C = 100K$, $\dot{\delta}_C = 50\mu m$, and $\dot{U}_C = 0.7$ m/s.

Figure 7 shows a transition line, which delimits the sharp transition between the gouging region and the trailing region. Experiments indicate that this line moves toward the rear as the current increases (Refs. 2, 9). At the verge of humping, the trailing region receives little heat from the arc and contributes very little to weld penetration; thus, the transition line is located at the depth of maximum penetration, where the melting interface is close to horizontal.

The weld pool presents different configurations, depending on the welding parameters. These variations are the origin of weld pool geometric defects. In this work, the weld pool under high currents was analyzed by looking at welds where the current was suddenly stopped, in order to see the geometry of the gouging region. Traditional techniques, such as looking at cross sections of a weld joint do not provide enough information about the configuration of the weld pool. Figure 6 shows how the cross section of a good weld presents no obvious signs of the very depressed surface that occurs during the melting process. Given that the thin liquid layer of the gouging region solidifies almost instantly, there is no need to remove

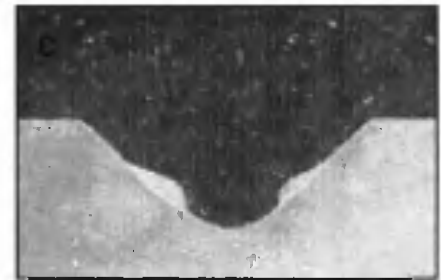
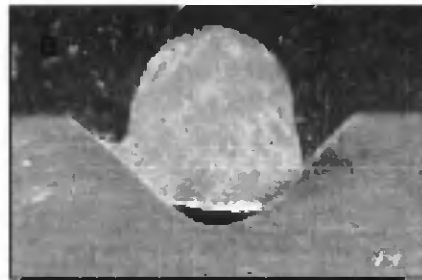
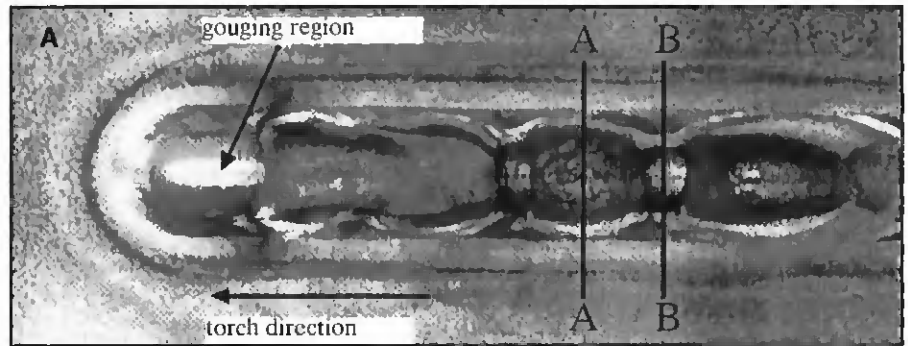


Fig. 1 — Humping in GTAW. A — Top view of the humped weld joint; B — cross section of the bead-like protuberance (cross section A-A); C — cross section of the void between beads (cross section B-B).

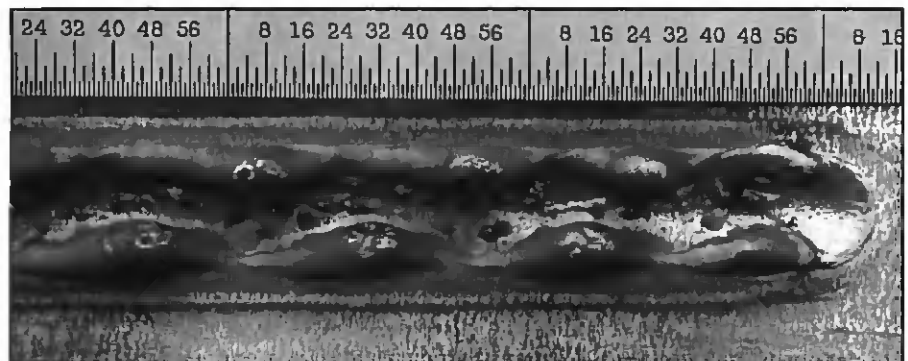


Fig. 2 — Parallel humping in GTAW. The two parallel lumped beads can be seen on the sides of an empty groove.

the molten metal by impulsive methods involving a hammer blow (Ref. 19), a gun blast (Ref. 15), or a mechanical ejection rig (Ref. 16).

Penetration Mechanism

Because the weld pool turns into a thin film under the arc, the mechanism of heat transfer and penetration is very different from that of a weld pool at lower current and velocities, where recirculating flows dominate the heat transfer.

At lower currents, the weld pool experiences little free surface deformation, but does experience recirculating flows in the molten metal. Since convection is dominant in these cases (Ref. 17), these recirculating flows greatly affect the heat transfer in the weld pool, and thus weld penetration (Refs. 18–21).

In weld pools with recirculation, Marangoni forces are dominant, and surface-active elements such as sulfur are the main determinants of the direction and intensity of these flows (Refs. 21–23). Steels with less than 60 ppm of sulfur have outward flows, which make the molten metal act as an insulating layer, impeding heat transfer to the underlying solid metal. This causes wide welds with shallow penetration, as indicated in the first schematic of Fig. 8. Steels with a sulfur content above 70 ppm show inward flows, which cause deeper penetration and a narrower head, as shown in the second schematic of Fig. 8.

At high currents, the weld pool turns into a thin film with the free surface immediately adjacent to the underlying solid metal. This way the arc acts almost directly melting the solid metal as shown in the third schematic of Fig. 8. The heat content



Fig. 3 — Tunnel porosity in GTAW.

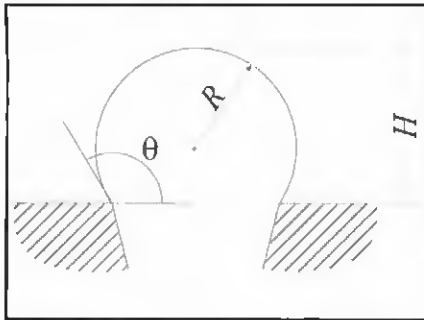


Fig. 5 — Cross section of a long cylindrical fluid body.

absorbed and transported by the molten metal is very small, heat transfer to the underlying solid is very efficient, and penetration increases. In this case, surface-active elements have little influence on penetration, suggesting a different mechanism of welding penetration is present.

To verify that in a thin weld pool the Marangoni forces are of little importance, a set of bead-on-plate welds was performed with the same conditions on 304 stainless steel, differing only on their sulfur content (6 ppm vs. 230 ppm). The welding parameters used in the experiments were such that these welds had a gouging region. The resulting welds were sectioned and etched, and penetration was measured. The results are shown in Fig. 9. Welding penetration does not change significantly with the sulfur content, indicating that the Marangoni forces have little effect at these high current levels. A slight decrease in penetration with sulfur content is observed at 500 A; a possible cause for this phenomenon is the interaction between the trailing region and the arc. At low-sulphur content, the trailing region is bulky and interacts with the arc when there is no humping; on the other hand, at high-sulphur content, there is an open gouging region that leaves an open space behind the arc. While this mechanism operates at all welding currents, the trailing region is much more prominent at high currents.

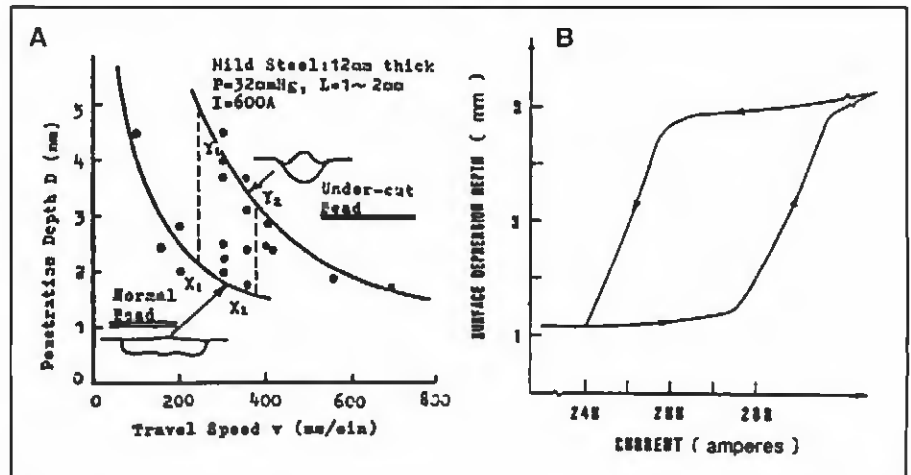


Fig. 4 — Sudden increase in penetration with travel speed (A [Ref. 1]) and with current (B [Ref. 3]). The location of the sudden change in penetration depends on the direction of the variation in current.

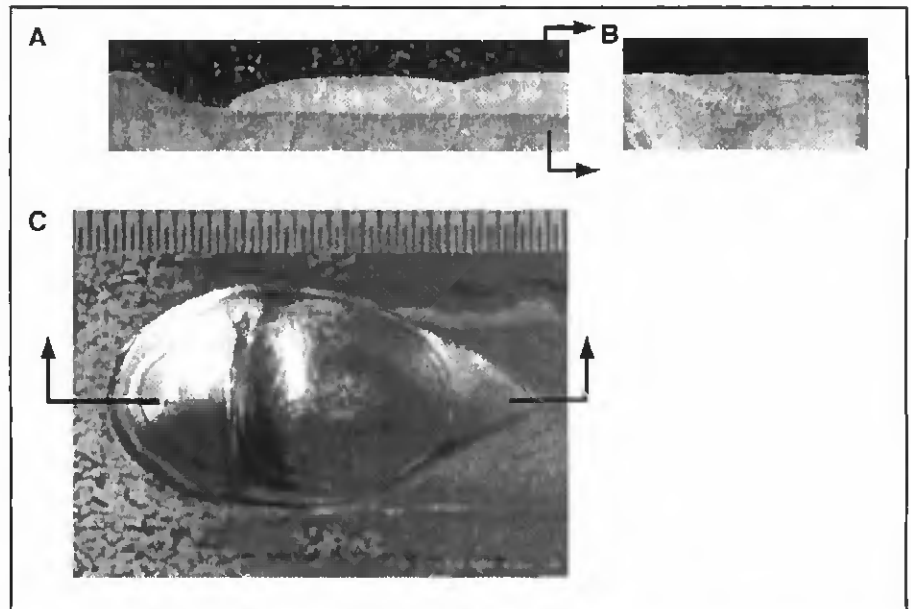


Fig. 6 — Weld pool at high currents and speeds. A — Longitudinal section; B — cross section; C — top view of a weld in which the welding current was suddenly cut off.

Fingerlike Penetration Paradox

Fingerlike penetration is well known in gas metal arc welding (GMAW), but it also occurs in GTAW. This type of penetration can be explained based on the enhanced heat transfer mechanism of a severely depressed weld pool surface.

In GMAW, the kinetic energy of the impinging droplets influences the recirculating flows in the weld pool, and thus the penetration. Spray transfer mode or electrode oscillation (Ref. 24) produce small and fast droplets, which cause in some cases the distinctive weld cross section shown in Fig. 10. The paradox is that similar cross sections are observed in GTAW

at high current, but they cannot be explained based on droplet impingement.

The explanation of this paradox is that in GTAW at high currents, the finger is caused by the efficient heat transfer of the arc through the thin liquid layer, while the width of the weld bead is given by the melting effect of the hot metal surrounding the gouging region. This mechanism is consistent with experimental observations by Ishizaki (Ref. 9).

This mechanism also explains the depth of the finger penetration in GMAW in those cases in which the depth of penetration cannot be explained by the heat content and momentum of impinging droplets of molten metal.

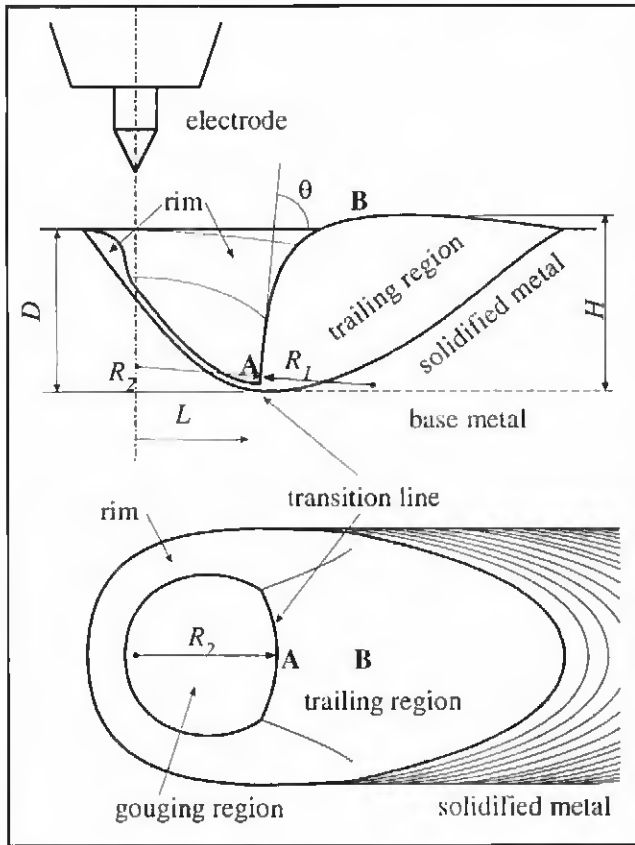


Fig. 7 — Weld pool at high currents and speeds. The free surface is very depressed, turning into a thin liquid film under the arc. A thicker rim of liquid runs around the edge of the weld pool carrying molten metal to the bulk of liquid at the rear of the weld pool. The transition line marks the abrupt change from the thin liquid film into the bulk of liquid at the rear.

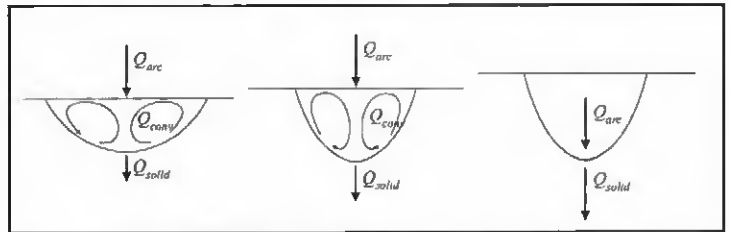


Fig. 8 — Penetration mechanism: left — outward recirculating flows for low-sulfur steel; center — inward recirculating flows for high-sulfur steel; right — no recirculating flows; the arc acts almost directly over the front of penetration.

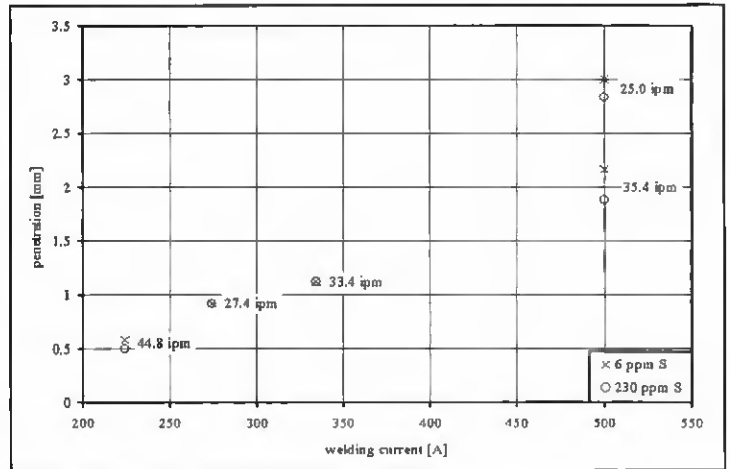


Fig. 9 — Welding penetration at high current. Welding penetration varies very little with sulfur content, indicating that Marangoni forces are not dominant in this regime.

Heat Transfer Mode

For fast moving heat sources, the relative motion between heat source and substrate dominates heat transfer, with heat conduction playing a secondary effect. A heat source is considered fast when the Peclet number is larger than one. The Peclet number is defined as:

$$Pe = VL/\alpha \quad (4)$$

where V is the welding speed, L is the characteristic length of the heat source (e.g., the arc diameter), and α is the heat diffusivity of the solid substrate. The values for Pe for the experiments considered in this paper range between 35 and 75, indicating that the heat transfer problem can be approximated as one dimensional in the direction of penetration, with the following energy balance at the melting interface:

$$Q_a(x) = \rho\Delta H_m W(x) + Q_{solid}(x) \quad (5)$$

where x is a longitudinal coordinate, as indicated in Fig. 7; $Q_a(x)$ is the heat input from the arc; ΔH_m is the latent heat of melting; $W(x)$ is the velocity at which the melting interface advances, creating the welding

penetration; and $Q_{solid}(x)$ is the heat flow from the melting interface to the solid substrate. Equation 5 can be integrated over the longitudinal coordinate x , which is proportional to the residence time of the arc. Assuming a Gaussian heat source with symmetry of revolution, and considering the effective diameter of the heat source as four times its standard deviation σ_Q , it is possible to estimate the average heat transfer into the solid (\bar{Q}_{solid}) as follows:

$$\bar{Q}_{solid} = \frac{\sqrt{2\pi}}{4} Q_{max} - \frac{\rho\Delta H_m DV}{4\sigma_Q} \quad (6)$$

where D is the depth of weld penetration. This equation provides an order of magnitude estimation of the thermal energy that diffuses into the solid beyond the melting interface. For a typical case, the latent heat of melting plays a small role in the energy balance. The typical values of \bar{Q}_{solid} range around 3×10^7 W/m².

Humping Mechanism

The small thickness of the liquid film in the gouging region implies that it will solidify very quickly where there is not

enough heat from the arc. We showed above that heat transfer in the solid creates a heat loss \bar{Q}_{solid} , which is of the order of magnitude of the maximum heat input from the arc (Q_{max}). The heat capacity of the thin layer in the gouging region is given by the heat capacity of the overheated liquid metal plus the latent heat of melting, which can be approximated as $(c_p \hat{T}_C/2 + \Delta H_m)\rho\delta_C$. A time scale for the solidification of the gouging region can be estimated as

$$\begin{aligned} \text{time scale for solidification} \\ = \left(\frac{c_p \hat{T}_C}{2} + \Delta H_m \right) \frac{\rho\delta_C}{\bar{Q}_{solid}} \quad (7) \end{aligned}$$

where c_p and ΔH_m are the specific heat and latent heat of melting of the molten metal. A typical value for the time scale for solidification is of the order of a few milliseconds. Such rapid solidification indicates that if the gouging region extends to a point where there is not enough heating from the arc, the gouging region will solidify, starting the humping process.

Figure 11 illustrates schematically this process. Figure 11A shows a weld pool in which the gouging region does not extend

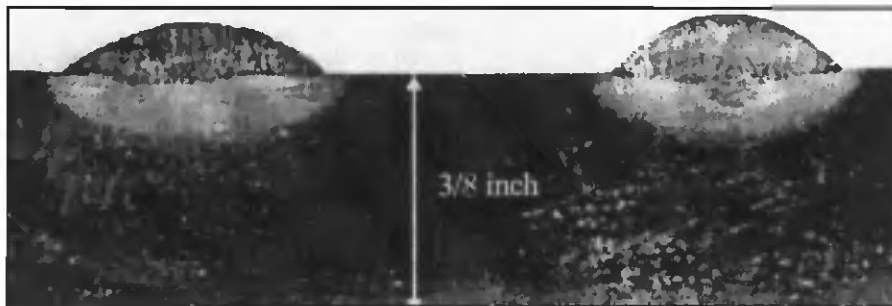


Fig. 10 — Penetration in GMAW. Both welds have been produced under the same conditions, but for the weld on the right, the electrode was oscillated to detach the droplet, showing fingerlike penetration (Ref. 24).

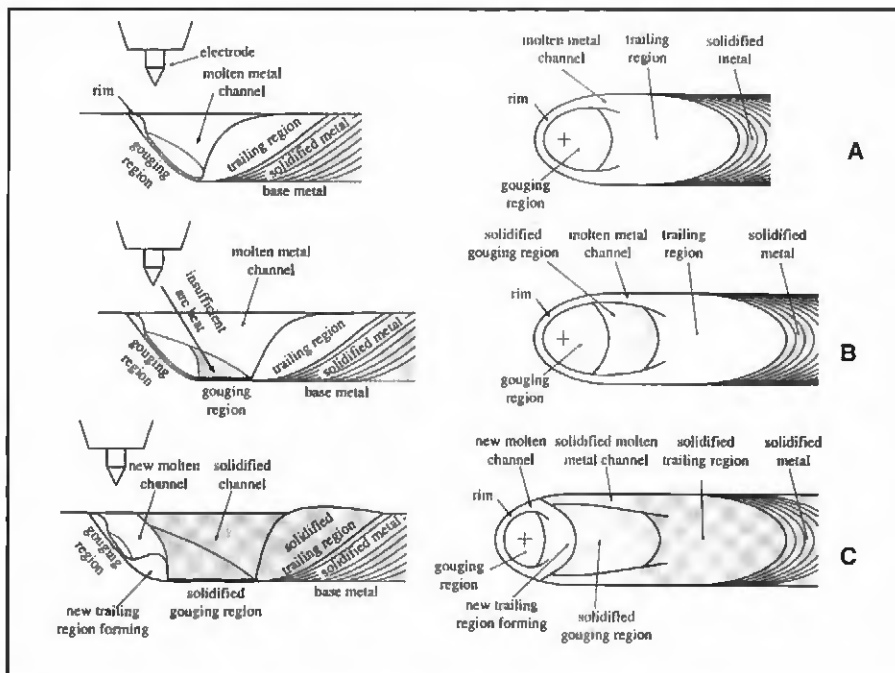


Fig. 11 — Humping formation in GTAW. A — The gouging region does not extend outside the hot region of the arc, the thin liquid layer and the side channels feed the trailing region, and humping does not happen. B — The trailing region is far from the arc and the thin liquid layer solidifies prematurely. The trailing region is fed by two molten metal channels surrounding the gouging region. C — The side channels start to solidify and stop feeding the trailing region, which also begins to solidify. A new humped bead starts to form.

far from the arc, therefore the thin liquid layer feeds the trailing region, and humping does not occur. Figure 11B represents a weld pool in which the trailing region starts far from the arc. In this case, the farther portion of the gouging region does not receive enough heat from the arc, and solidifies almost instantly. The trailing region is fed by two molten metal channels, one on each side of the weld, surrounding the gouging region with a rim of molten metal. Figure 11C shows the evolution of the weld of Figure 11B. The side channels start to solidify, and stop feeding the trailing region, which also begins to solidify. With no possibility of transferring molten metal to the rear of the weld pool a new humped bead starts to form.

In summary, the location of the transition line is critical; humping will occur when the transition line is pushed far enough toward the rear of the weld pool into the region where the heat from the arc is insufficient to prevent solidification of the film of molten metal.

In order to calculate the threshold for humping, knowledge of all of the forces involved at the weld pool is necessary. Forces like surface tension will also be dependent on the geometry of the free surface making this a very difficult calculation. A simplified estimation which captures the relevant characteristics of the generation of humping is presented below. These predictions are compared against experiments later in this paper.

Forces Acting on the Transition Line

The location of the transition line (point A in Fig. 7) is determined by a balance of the forces acting on it. These forces are hydrostatic pressure, capillary pressure, and arc pressure.

The hydrostatic forces are originated by the pressure due to the column of metal (H in Fig. 7) between the center point of the transition line (point A) and the highest point of the free surface (point B). Their value at point A is

$$(P_h)_A = \rho g H \quad (8)$$

where ρ is the density of the molten metal, and g is the acceleration of gravity (9.81 m/s^2). The capillary forces act over all of the free surface, and at point A their value is

$$(P_c)_A = \sigma \left(\frac{1}{R_1} + \frac{1}{R_2} \right) \quad (9)$$

where σ is the surface tension and R_1 and R_2 are the principal curvatures of the free surface at the transition line, as shown in Fig. 7. The radius of curvature R_1 belongs to the plane of symmetry, and R_2 belongs to a plane normal to the plane of symmetry and to the free surface at point A. At point B, the surface has generally much smaller curvature as shown by the photograph of Fig. 6. The simple appearance of Equation 9 is misleading because the curvatures of the free surface can be positive or negative and are very difficult to measure or predict.

At the verge of humping, the transition line is at the edge of the arc with the trailing region behind, so very little influence from the arc is expected at point B. For this reason, it is assumed here that near the onset of humping, $(P_a)_B \approx 0$.

Many other forces act on the trailing region, such as thermocapillary Marangoni forces, electromagnetic, and buoyancy. These forces are induced by the action of the arc, which on the verge of humping is very weak over the trailing region. For this reason, these forces are expected to be of little importance for influencing the occurrence of humping.

Force Balance at the Transition Line

The location of the transition line can be determined by a force balance. In this simplified analysis, the forces to be considered are the arc pressure (P_a), the hydrostatic pressure (P_h), and the capillary pressure (P_c). A force balance involving points A and B in Fig. 12 can be written as:

$$(P_a + P_h + P_c)_A = (P_a + P_c)_B \quad (10)$$

As mentioned in the previous section,

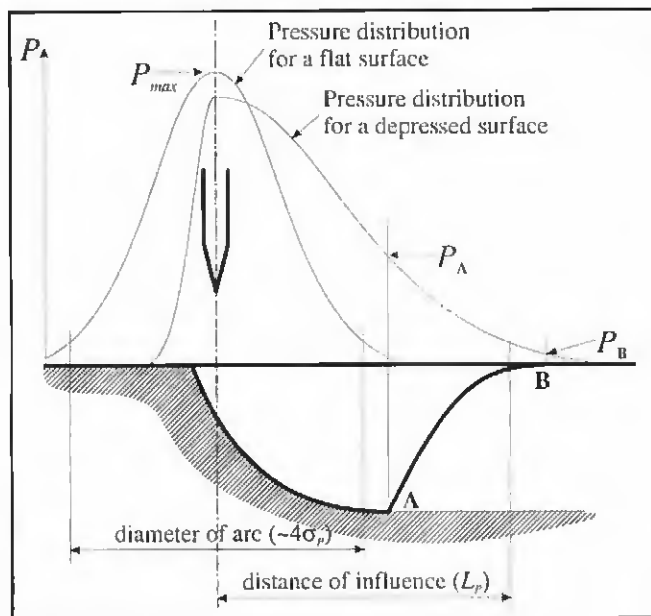


Fig. 12 — Arc pressure distribution for a very depressed surface.

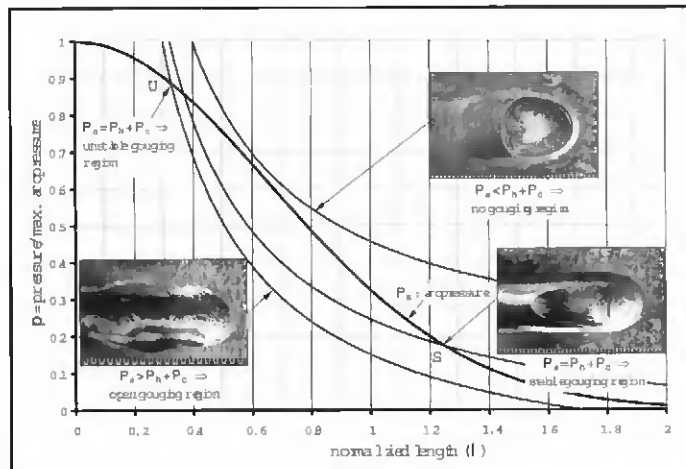


Fig. 13 — Stability of the gouging region. The bell-shaped curve represents the arc pressure, the other three curves represent the pressure in the metal at the transition line. Top curve: metal pressure exceeds arc pressure and there is no gouging region. Intermediate curve: intersects arc pressure at unstable point U and at stable point S, which determines the extension of the gouging region. Bottom curve: intersects arc pressure only at unstable point, beyond which arc pressure dominates opening up the gouging region, and generating a split bead.

the forces acting at point B are very small and will not be considered in this analysis. The force balance can be expressed in a nondimensional form using scaling relationships that relate an unknown quantity such as a curvature to a known quantity of the same order of magnitude. The shape of the pressure and heat input distribution for an arc over a deformed surface will be discussed later.

The radius R_1 can be scaled with that of a circle in the plane of symmetry with tangents at the transition line (point A) and highest point (B), as indicated in Fig. 7. The radius R_2 typically has its center outside the molten metal, and for this reason it is negative. This radius will be scaled with a circle with center in the axis of revolution of the electrode. The plane of this circle is perpendicular to the free surface at the center of the transition line. The size of the gouging region (L) will be scaled with the pressure length scale of the arc (L_p). The arc pressure will be scaled with its maximum value. For heat transfer calculations, the heat input from the arc will be scaled with the average heat transfer into the solid (\bar{Q}_{solid}). This last scaling relationship is useful for determination of the onset of humping. Welding penetration occurs when the heat of the arc is larger than the heat into the solid, and the liquid will solidify when the heat from the arc is less than the heat transfer into the solid.

From the above considerations, the following set of scaling relationships is obtained:

$$R_1 = \frac{H}{2\sin^2(\theta/2)} r_1 \quad (11)$$

$$R_2 = -\frac{L}{\sin(\theta)} r_2 \quad (12)$$

$$L = L_p l \quad (13)$$

$$P_a(L) = P_{max} p_a(l) \quad (14)$$

$$Q_a(L) = \bar{Q}_{solid} q_a(l) \quad (15)$$

where the dimensionless factors r_1 , r_2 , l , $p_a(l)$, and $q_a(l)$, are expected to be of the order of magnitude of 1 because they relate two quantities of the same order of magnitude. In these scaling relationships the uppercase symbols correspond to magnitudes with dimensions, and the lower case symbols correspond to dimensionless magnitudes.

Applying the above scaling relationships and rearranging the terms, a nondimensional form of Equation 10 has the following form:

$$p_a(l) = \frac{\rho g H}{P_{max}} - \frac{2\sigma}{HP_{max}} \frac{\sin^2(\theta/2)}{r_1} + \frac{\sigma}{L_p P_{max}} \frac{\sin(\theta)}{r_2 l} \quad (16)$$

Equation 16 can be represented graphically as in Fig. 13. The left member represents the normalized arc pressure ($p_a(l)$), and the right member represents the metal pressure (hydrostatic plus capillary). When the curves representing both terms as a function of l (normalized size of the gouging region) intersect, they determine a point of equilibrium for the transition line.

In Fig. 13, the arc pressure is represented as a Gaussian with its center at the beginning of the gouging region. This is only a coarse approximation since the true shape of the pressure distribution is not well known; however, it is reasonable to assume that the arc pressure at the transition line decreases with distance from the electrode. The other three curves represent combined normalized hydrostatic and capillary pressures (metal pressure) for three possible situations, absence of a gouging region, unstable equilibrium, and stable equilibrium.

Stability of the Gouging Region

When metal pressure is higher than the arc pressure at all times, there is no gouging region. If a fluctuation created one, the forces in the metal would overcome the arc pressure and close the incipient gouging region.

When the metal pressure crosses the pressure curve twice, there are two points at which the metal and arc forces are in equilibrium. One of these points (point U in Fig. 13) is unstable because any fluctuation that increases the size of the gouging region will increase the relative force of the arc, expanding the gouging region even further, until it reaches a stable point. A fluctuation that decreases the size of the gouging region will create a force balance favorable to the metal pressure, closing the gouging region. At the stable point (point S), a fluctuation that increases the gouging region also increases the closing forces (metal pressure minus arc pressure), and a fluctuation that tends to decrease the gouging region increases

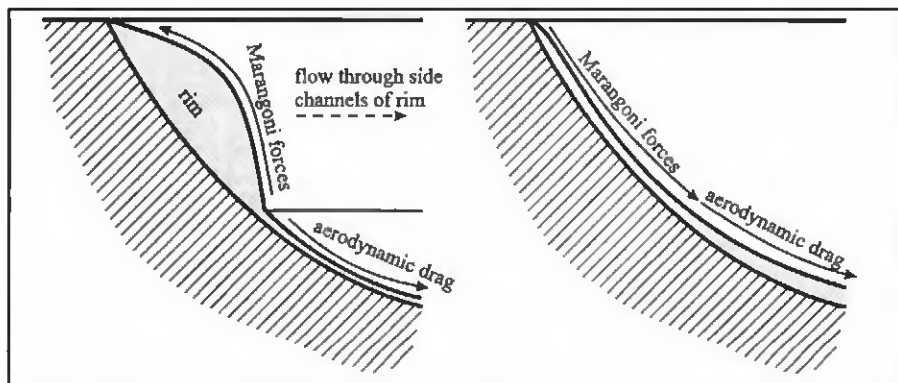


Fig. 14 — Detail of the front of the weld pool. The left figure corresponds to steel with low sulfur, when Marangoni forces create a rim. The figure at right corresponds to steel with high sulfur, when no rim is created.

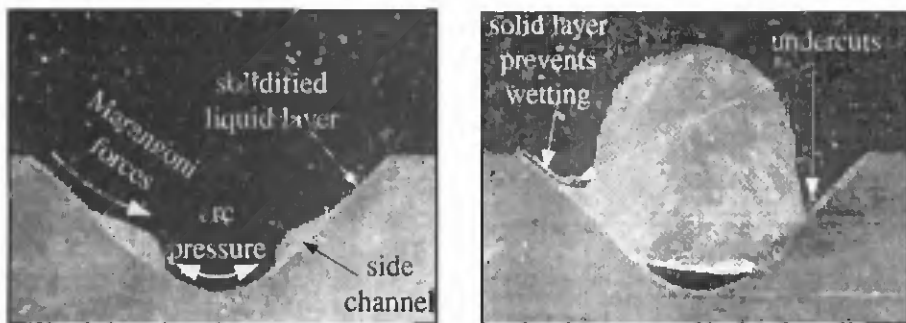


Fig. 15 — Undercutting mechanism. In high S steel, Marangoni forces cause a thin liquid layer that solidifies prematurely and prevents wetting, causing undercutting.

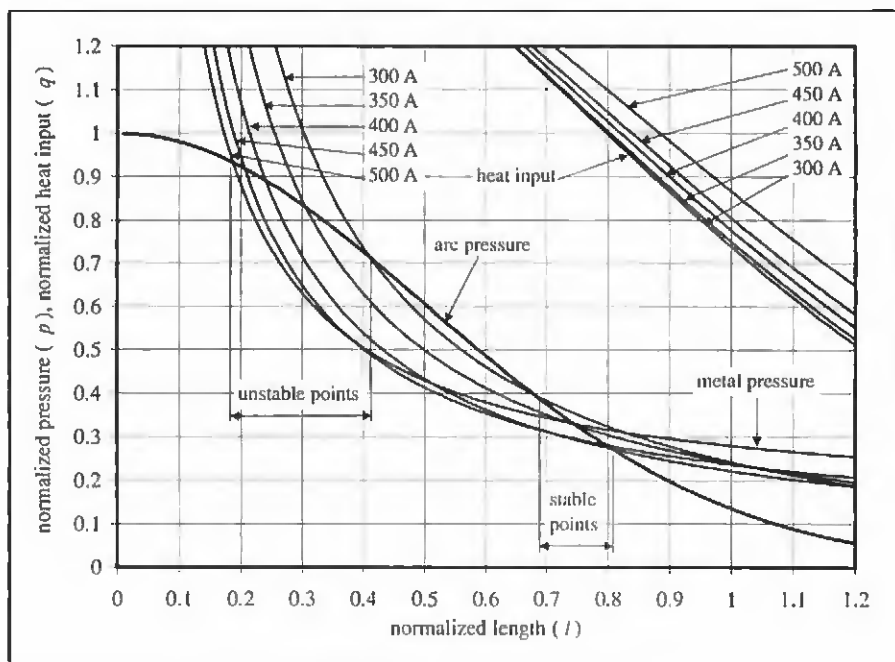


Fig. 16 — Force balance at the transition line at the onset of humping calculated using Equation 16 and data by Savage (Ref. 8) and Choo (Ref. 20).

the opening forces (arc pressure minus metal pressure).

The third possible case is when the metal pressure crosses the arc pressure curve only once. The crossing point is unstable, and the arc pressure is always larger than the metal pressure. The arc force pushes the transition line ever further, and the trailing end of the weld pool breaks into two parallel streams that will originate the defects of split bead, parallel humping, and tunnel porosity.

Increases in welding current with a constant metallostatic head decrease the metal pressure curve by approximately a constant factor (only P_{max} is significantly affected). Increases in the metallostatic head (closely related to increases in penetration) shift the metal pressure curve upward in a parallel way (only H is significantly affected). When the metal pressure decreases, the transition line moves toward the rear. Therefore, an increase in current or a decrease in metallostatic head will expand the gouging region.

Undercutting Mechanism

The configuration of the rim around the gouging region can explain why steel with higher sulfur content tends to suffer more undercutting, why this defect appears when welding at high speeds, and why undercutting increases slightly with arc length (Ref. 21).

The rim is not always present, and its configuration depends on the amount of sulfur in the substrate. This has been observed in AISI 304 stainless steel with sulfur content of 6 ppm and 50 ppm but not when the sulfur content is 230 ppm. This finding suggests that Marangoni forces are more important than aerodynamic shear at the rim.

For steels with low sulfur content, the surface tension of the molten metal decreases with temperature (Ref. 25); therefore, the molten metal at the front of the gouging region flows in the direction of welding, and the rim is formed to transport that liquid to the trailing region. For high sulfur content, the Marangoni forces act in the opposite direction, and the molten metal is transported to the rear of the weld pool through the gouging region — Fig. 14. For intermediate content of sulfur, there was still a rim, but the Marangoni forces pushed it toward the root of the weld. Gravity is also likely to play a role in pushing the rim downward.

Figure 15 shows the cross section of a weld on AISI 304 with 50 ppm of S; this amount of sulfur generates Marangoni forces in the opposite direction to that in a pure metal. These forces drive the liquid in the side channels of the rim away from the side of the weld bead, generating a thin

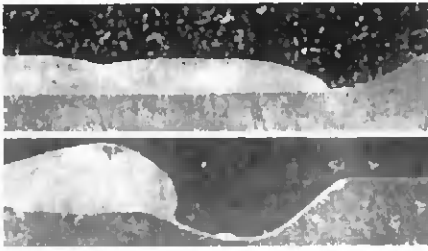


Fig. 17—Apparent contact angle for low and high sulfur in AISI 304. The sulfur content of the base metal is 6 ppm for the picture on top, and 230 ppm for that on the bottom. The trailing region with higher sulfur content is less wetting.

liquid layer, susceptible of premature solidification, similar to what occurs in the generation of humping. The solidification of this thin liquid layer stops the wetting of the side of the weld bead, causing undercutting. If the base material has low sulfur, the Marangoni forces would push liquid toward the side of the weld bead, preventing the formation of a thin liquid layer, thus preventing undercutting.

Lower welding speeds with recirculating flows in the weld pool would be less susceptible to undercutting because there is no gouging region. Increasing the arc length could reduce slightly the pressure at the bottom of the gouging region, thus letting the side channels of the rim sink deeper into the gouging region and increasing undercutting.

Comparison with Experimental Results

The mechanism for humping stated above can be compared with the measurements of the onset of humping by Savage et al. (Ref. 8). In that work, the position of the transition line and arc size were not reported, and will be estimated here. In order to accomplish this, knowledge of the relevant properties of the arc are necessary.

For a flat surface, the arc pressure has symmetry of revolution, with a distribution profile resembling that of a Gaussian distribution, as measured by Lin (Ref. 3). Very little is known about the behavior of a welding arc on very irregular geometries such as those encountered on very depressed weld pools in traveling welds. In these cases, the symmetry of revolution is broken and the arc force is expected to increase with the deformation (Ref. 26). In all cases, it is reasonable to assume the arc pressure on the free surface decreases with distance from the electrode, as shown in Fig. 12. Also, the depression of the weld pool should skew the pressure distribution curve, making it shorter on the front and expanding it at the rear. The maximum pressure over the inclined surface should be somewhat smaller but of the same

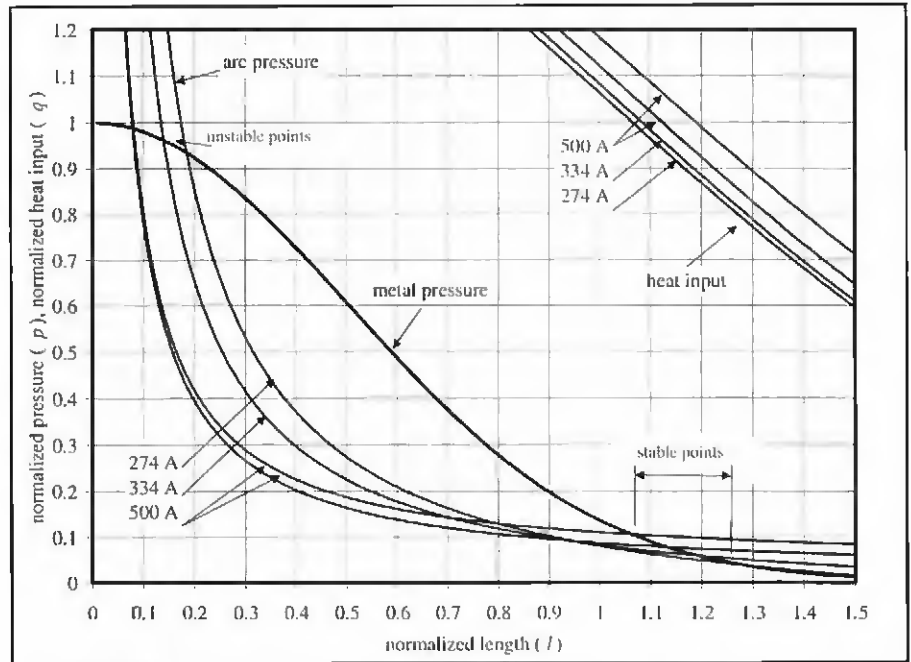


Fig. 18—Force balance at the transition line at the onset of humping. These curves have been calculated using Equation 16 and experimental data for low sulfur summarized in Table 5. These experiments are in agreement with Fig. 16.

order of magnitude as on a flat surface. The heat input from the arc over a deformed surface is expected to be similarly skewed.

In the absence of specific measurements or models of the arc pressure on a deformed surface, the maximum arc pressure and heat input will be assumed to be the same as those on a flat surface. The distribution profile on a deformed surface will be assumed to be half a Gaussian distribution but twice as broad as for a flat surface, as indicated in Fig. 12. If the pressure length scale for a flat surface is approximately $2\sigma_p$ (i.e., over a flat surface, the pressure of an arc is felt within a circle of radius $2\sigma_p$), the pressure length scale of the arc over a deformed surface will be

$$L_p = 4\sigma_p \quad (17)$$

Since our estimations of arc properties on a deformed surface are based on an arc over a flat surface, we will focus momentarily on that simpler type of arc. The Gaussian distribution approximations for the arc pressure and the heat input over a flat surface have the following expressions:

$$P_{flat}(L) = P_{max} \exp\left(-\frac{L^2}{2\sigma_p^2}\right) \quad (18)$$

$$Q_{flat}(L) = Q_{max} \exp\left(-\frac{L^2}{2\sigma_Q^2}\right) \quad (19)$$

where L is the radial distance from the axis of symmetry. P_{max} and Q_{max} are the maximum values and σ_p and σ_Q are the standard deviation of the distributions. The normalized expression of these equations is as follows:

$$p_a(l) = \exp(-2l^2) \quad (20)$$

$$q_a(l) = \frac{Q_{max}}{Q_{solid}} \exp\left(-2\frac{\sigma_p^2}{\sigma_Q^2} l^2\right) \quad (21)$$

The parameters for a flat surface can be estimated by performing regressions on the data from Lin (Ref. 27) for pressure and Tsai (Ref. 28) for heat input.

For pure argon, electrode tip angles between 30 and 60 deg, welding currents between 300 and 600 A, and arc lengths between 2 and 8 mm, the parameters for a Gaussian fitting of Lin's experimental data can be approximated by the following equations:

$$P_{max} = 32.85I^{1.244}\alpha_e^{-0.7855} \quad (22)$$

$$\sigma_p = 1.784 \cdot 10^{-4} I^{0.2892} \alpha_e^{0.1571} \quad (23)$$

where I is the welding current in amperes, α_e is the electrode tip angle in degrees, P_{max} is in pascals, and σ_p is in meters. The pressure distribution is independent from the arc length within the experimental error in the range measured.

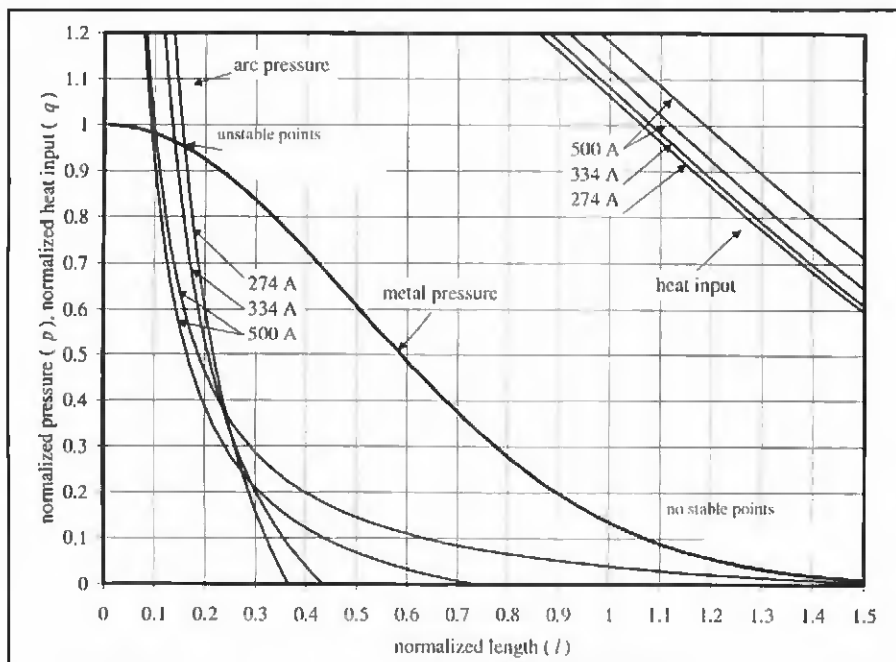


Fig. 19 — Force balance for open gouging region. These curves have been calculated using Equation 16 and experimental data for high sulfur summarized in Table 5.

For a pure argon arc, with an electrode tip angle of 75 deg, for welding currents between 100 and 280 A and for arc lengths between 2 and 9 mm, the parameters for a Gaussian fitting of Tsai's experimental data can be approximated by the following equations:

$$Q_{max} = 1.441 \cdot 10^4 l^{0.7444} L_a^{-0.7680} \quad (24)$$

$$\sigma_Q = 3.770 \cdot 10^{-3} l^{0.2645} L_a^{0.3214} \quad (25)$$

where L_a is the arc length in meters, Q_{max} is in watts per meter squared, and σ_Q is in meters.

The relevant information from Savage's work is summarized in Tables 2 and 3 and in Fig. 16. The normalized extension of the gouging region at the onset of humping (l_{eq}) was determined from Equation 16 considering the arc pressure as a Gaussian function (Equation 18), with its parameters given by Equations 22 and 23. The apparent angle of contact was assumed to be 90 deg. The normalized radii r_1 and r_2 must be of the

order of magnitude of one. The calculations are very sensitive to these parameters, and values of $r_1=1$ and $r_2=0.4$ were chosen because they best represented the threshold of humping for Savage's data.

The curves of normalized heat input (q_a) in Fig. 16 were obtained assuming the heat input as a Gaussian function (Equation 19) with parameters given by Equations 24 and 25. The normalization parameter is the average heat input into the solid, given by Equation 6.

Figure 16 shows that between 300 and 500 A, the transition line at the onset of humping is always located at approximately the same place in normalized coordinates. This place is located between $l=0.68$ and $l=0.81$. These values correspond to a normalized heat input also within a narrow range (between 1.01 and 1.17). This supports the hypothesis that at high currents, humping occurs when the transition line extends beyond the reach of the arc (indicated by $q_a=1$).

Figures 18 and 19 represent experi-

Table 2 — Parameters Used in Experiments of Fig. 16

S content (ppm)	400
ρ (kg/m ³)	7000
σ (N/m)	1.15
θ (degrees)	90
α_z (degrees)	90
ΔH_m (J/kg)	2.65×10^5

ments carried out in this investigation. The conditions for these experiments are summarized in Tables 4 and 5.

These welds were performed on 2-in.-wide \times 0.5-in.-thick AISI 304 bars that were cleaned with 120-grit sandpaper and then degreased with water and detergent. The electrode was $\frac{1}{8}$ -in.-diameter, 2% thoriated tungsten with 0.5-in. electrode extension from the ceramic nozzle. The distance from electrode tip to workpiece was $\frac{1}{4}$ in. Shielding was 100% Ar, with a flow of 30 ft³/h. Before each weld, the electrode was ground to a sharp end of 45 deg and preworn by doing ten 10-second spot welds at 300 A.

The apparent contact angle was visually estimated during welding as 90 deg for high-sulfur steel and 30 deg for low-sulfur steel. We observed that at the onset of humping, high-sulfur steel (230 ppm) produces less wetting on the base material than low-sulfur steel (6 ppm). Figure 17 shows longitudinal sections of interrupted welds on AISI 304 with 6 ppm sulfur content (top) and 230 ppm (bottom). The difference in wetting behavior with sulfur is evident.

Figure 18 corresponds to a set of welds performed on 304 stainless steel with 6 ppm S. These welds had a gouging region-but did not show humping. The normalized heat input at the transition line for these welds varies between 0.78 and 1.12, which is consistent with the values estimated for Savage's experiments.

Figure 19 corresponds to welds on 304 stainless steel with 230 ppm S. In this case, the molten metal is less wetting, lowering the metal pressure. This figure shows that the metal pressure is lower than the arc pressure, predicting an open gouging region, in agreement with the experiments performed.

Table 3 — Experimental Data, Calculated Arc Parameters, and Transition Line Conditions for the Construction of Fig. 16

I (A)	V (mm/s)	L_a (mm)	H (mm)	D (mm)	P_{max} (kPa)	σ_P (mm)	Q_{max} (W/mm ²)	σ_Q (mm)	\bar{Q}_{solid} (W/mm ²)	l_{eq}	q_{eq}
300	9.58	4.1	3.4	1.7	1.2	1.9	68	2.9	40	0.68	1.16
350	8.39	4.4	3.9	2.0	1.4	2.0	73	3.1	44	0.75	1.07
400	7.76	4.7	4.2	2.3	1.7	2.1	76	3.3	45	0.81	1.01
450	6.36	5.2	5.0	2.8	1.9	2.1	78	3.5	46	0.80	1.05
500	4.61	6.2	6.6	3.8	2.2	2.2	73	3.8	44	0.74	1.17

Discussion

The good agreement between the proposed humping mechanism and the experimental data from Figures 16, 18, and 19 is encouraging; however, many important factors in the calculation, such as the arc behavior over a very deformed surface, were unknown and needed to be estimated. For a more accurate understanding, further experiments and modeling are necessary. The prediction of the onset of humping could be more general if the metallostatic head could be calculated instead of being considered as an input of the problem. Predictions of the metallostatic head would help to produce a process envelope of great practical use, similar to that presented in Ref. 8.

A calculation of the curvatures of the free surface would also increase accuracy, especially for welds showing a gouging region at currents below 250 A. For these cases, quantitative predictions of the onset of humping were unreliable.

The sulfur content of the material affects the apparent contact angle of the trailing region, thus determining the presence or absence of humping in some critical cases (low sulfur helps prevent humping). The reason for the influence of sulfur on contact angle is not well understood. Given that the front of the trailing region is not in thermodynamic equilibrium, it is possible that Marangoni forces play a role.

Humping in GMAW

Bradstreet (Ref. 5) described the weld pool of GMAW under high current as composed of three streams of molten metal. Two of these, on each side of the depression, are equivalent to the side channels of the rim described in Fig. 7. The third stream, running parallel and between the other two, corresponds to molten filler metal. Between each of these streams, there is a gouging region susceptible to premature solidification. Given this similarity, the criterion for the onset of humping and the mechanism of penetration at high currents is likely to be valid for GMAW. The similarity between GMAW and GTAW defect formation is also emphasized by Shimada (Ref. 2), who calls the defect with an open gouging region "MIG-type humping bead."

Tunnel Porosity

An open gouging region can also cause the tunnel porosity shown in Fig. 3. In an open gouging region, the bottom of the weld pool solidifies prematurely and liquid metal accumulates in two streams on each side of the gouging region, as shown in Fig. 2. The solidified bottom prevents

Table 4 — Parameters Used in Experiments of Figs. 18 and 19

S content (ppm)	ρ (kg/m ³)	σ (N/m)	θ (degrees)	α_c (degrees)	ΔH_m (J/kg)
6	6900	1.82	30	60	2.65×10^5
230	6900	1.25	90	60	2.65×10^5

Table 5 — Experimental Data, Calculated Arc Parameters, and Transition Line Conditions for the Construction of Figs. 18 and 19. For all these cases $D = H$.

S content (ppm)	I (A)	V ($\frac{\text{mm}}{\text{s}}$)	L_c (mm)	H (mm)	l_{eq} —	q_{eq} —
6	274	11.6	7.3	0.9	1.06	1.12
6	334	14.1	7.5	1.1	1.13	0.99
6	500	10.6	9.4	3.0	1.2	0.88
6	500	15.0	8.5	2.2	1.29	0.78
230	274	11.6	7.3	0.9	—	—
230	334	14.1	7.5	1.1	—	—
230	500	10.6	9.2	2.8	—	—
230	500	15.0	8.2	1.9	—	—

the side streams from advancing and merging into a single liquid trailing region. When the side streams are too large, they collapse onto each other, forming a single trailing region. The bottom of this trailing region cannot be filled with molten metal because the collapsed channels cannot wet the prematurely solidified gouging region. This unfilled region becomes a tunnel-like pore upon solidification.

A similar mechanism can explain the formation of parallel tunnel porosity observed by Bradstreet (Ref. 5) in GMAW. In this case there are three parallel molten metal streams separated by two open gouging regions: two on the sides formed by the melting of the base material and a central stream corresponding to the filler material from the electrode. In this case, two parallel tunnels are formed when the side streams collapse over the central stream.

Use of Twin or Tandem Torches

Our findings suggest an explanation for the success of tandem torches for welding heavy sections. By splitting the current between two torches, the maximum arc pressure decreases, moving the transition line closer to the hot region of the arc, thus preventing the formation of defects. This explanation is consistent with the observations described in Ref. 29.

Conclusion and Recommendations

High-current arc welding is characterized by a very deep weld pool depression (gouging region), where the molten metal under the arc turns into a thin film that flows toward a bulk of liquid (trailing region) at the rear of the weld pool. This

large depression is the direct cause of several weld pool defects such as humping, undercutting, split bead, parallel humping, and tunnel porosity.

A balance of forces at the transition line between the gouging and trailing regions determines how far toward the rear the gouging region extends. When the thin liquid film of molten metal extends beyond the region heated by the arc, it solidifies, generating a defect. The location of the transition line relative to the size of the region heated by the arc can be estimated using Equation 16.

Premature solidification of the thin liquid layer at the side edge of the weld causes undercutting. Since Marangoni forces are relevant in that part of the weld, surface-active elements in the base metal affect the amount of undercutting. For example, steel with high sulfur content shows more undercutting than low-sulfur steel. In GMAW, the sulfur content of the electrode is unlikely to be of influence at high currents, because there is little mixing with the base metal in the gouging region.

Stainless steel with lower sulfur has a faster welding speed limit than steel with high sulfur. Switching to low-sulfur steels (of the order of 6 ppm) dramatically improves welding conditions. The beneficial effect of low sulfur at high currents is remarkable, especially when considering that at lower currents, steels with higher sulfur are preferred for their deeper welding penetration.

One important difference observed in the welding of steels with different amounts of sulfur is that the apparent contact angle of the trailing region produces less wetting for high sulfur than for low sulfur. This affects the capillary forces, shifting the balance toward larger gouging

regions, thus generating humping. The effect of additives in the metal or in the shielding gas is an unexplored area that could yield important results.

Productivity can be enhanced by using the forehand technique. In this technique, the welding torch is tilted in such a way that the plasma jet has a velocity component in the direction of motion of the torch. The main effect is to lower the arc pressure that is pushing the transition line into the cold region. This beneficial effect of the forehand technique was observed by Bradstreet (Ref. 5) and Shimada (Ref. 2).

If the workpiece was inclined so that the welding direction is downward, it is reasonable to expect that gravity forces (which push the transition line toward the hot region) would become more important, and the welding speed limit would be increased. Additional experiments would be necessary to test this hypothesis, since no studies about such a technique have been reported in the welding literature.

Another possibility for improving welding productivity would be to modify the arc behavior, such that the arc pressure at the transition line decreases, but the hot region remains approximately the same. More knowledge of the welding arc is necessary for effectively implementing this. Blunt GTAW electrodes generate less pressure than sharp ones at the same currents (Refs. 30, 31); therefore, using blunt electrodes should increase the welding speed limit. This effect was experimentally observed by Savage (Ref. 8). A method for improving productivity by modifying the arc with magnetic fields was proposed by Grigorenko et al. (Ref. 32). The use of a different shielding gas could also reduce the arc pressure and heat distribution.

Acknowledgments

This work was supported by the United States Department of Energy, Office of Basic Energy Sciences. The authors would also like to acknowledge the help of Dr. Stan David of Oak Ridge National Laboratory, Krista L. Niece, and Don Galler for their assistance in the experimental stage of this project and Vasilios Nikou for his thorough proofreading of the draft.

References

1. Yamamoto, T., and Shimada, W. 1975. A study on bead formation in high speed TIG arc welding. *International Symposium in Welding*, Osaka, Japan.
2. Shimada, W., and Hoshinouchi, S. 1982. A study on bead formation by low pressure TIG arc and prevention of undercut bead. *Quarterly Journal of the Japan Welding Society* 51(3): 280-286.
3. Lin, M. L., and Eagar, T. W. 1985. Influence of arc pressure on weld pool geometry.

Welding Journal 64(6): 163-s to 169-s.

4. Gao, F., and Sonin, A. A. 1994. Precise deposition of molten microdrops: The physics of digital microfabrication. *Proc. R. Soc. Lond. A* 444: 533-554.
5. Bradstreet, B. J. 1968. Effect of surface tension and metal flow on weld bead formation. *Welding Journal* 47(7): 314-s to 322-s.
6. Gratzke, U., Kapadia, P. D., Dowden, J., Kroos, J., and Simon, G. 1992. Theoretical approach to the humping phenomenon in welding processes. *Journal of Physics D: Applied Physics* 25: 1640-1647.
7. Schiaffino, S., and Sonin, A. A. 1997. Formation and stability of liquid and molten beads on a solid surface. *Journal of Fluid Mechanics* 343: 95-110.
8. Savage, W. F., Nippes, E. F., and Agusa, K. 1979. Effect of arc force on defect formation in GTA welding. *Welding Journal* 58(7): 212-s to 224-s.
9. Ishizaki, K. 1962. Interfacial tension theory of the phenomena of arc welding — Mechanism of penetration. *Physics of the Welding Arc*. London, U.K.: The Institute of Welding, pp. 195-209.
10. Ishizaki, K. 1980. A new approach to the mechanism of penetration. *Weld Pool Chemistry and Metallurgy*, Vol. 1, Ed. N. Bailey. London, U.K.: The Welding Institute, pp. 65-76.
11. Demyantsevich, V. P., and Matyukhin, V. D. 1972. Characteristics of the movement of molten metal in the weld pool during welding with a nonconsumable electrode. *Svar. Proiz* (10): 1-3.
12. Matsunawa, A., and Nishiguchi, K. 1979. Arc behaviour, plate melting, and pressure balance of the molten pool in narrow grooves. *Arc Physics and Weld Pool Behaviour*, Vol. 1, pp. 301-310. London, U.K.: The Welding Institute.
13. Mendez, P. F., and Eagar, T. W. 2001. Estimation of the characteristic properties of the weld pool during high productivity arc welding. *Mathematical Modelling of Weld Phenomena 5*, Eds. H. Cerjak and H. K. D. H. Bhadeshia. London, U.K.: Institute of Materials, pp. 67-94.
14. Pierce, S. W., Burgard, P., and Olson, D. L. 1999. Thermocapillary and arc phenomena in stainless steel welding. *Welding Journal* 78(2): 45-s to 52-s.
15. Savage, W. F., Nippes, E. F., and Zanner, F. J. 1978. Determination of GTA weld-puddle configurations by impulse decanting. *Welding Journal* 57(7): 201-s to 210-s.
16. Wahab, M. A., and Painter, M. J. 1997. Numerical models of gas metal arc welds using experimentally determined weld pool shapes as the representation of the welding heat source. *International Journal of Pressure Vessels and Piping* 73: 153-159.
17. Rivas, D., and Ostrach, S. 1992. Scaling of low-Prandtl-number thermocapillary flows. *International Journal of Heat and Mass Transfer* 35(6): 1469-1479.
18. Matsunawa, A., Yokoya, S., and Asako, Y. 1987. Convection in weld pool and its effect on penetration shape in stationary arc welds. *Transactions of JWRI* 16(2): 1-8.
19. Zacharia, T., David, S. A., Vitek, J. M., and DebRoy, T. 1989. Weld pool development during GTA and laser beam welding of Type 304 stainless steel, Part I — Theoretical analysis. *Welding Journal* 68(12): 499-s to 509-s.
20. Choo, R. T. C., Szekely, J., and Westhoff,

R. C. 1990. Modelling of high current arcs in welding with emphasis on free surface phenomena in weld pool. *Welding Journal* 69(9): 346-s to 361-s.

21. Mills, K. C., and Keene, B. J. 1990. Factors affecting variable weld penetration. *International Materials Reviews* 35(4): 185-216.
22. Heiple, C. R., and Roper, J. R. 1982. Mechanism for minor element effect on GTA fusion zone geometry. *Welding Journal* 61(4): 97-s to 102-s.
23. Oprea, G. M., and Szekely, J. 1984. Heat and fluid flow phenomena in weld pools. *Journal of Fluid Mechanics* 147: 53-79.
24. Jones, L. A. 1996. Dynamic electrode forces in gas metal arc welding. Ph.D. diss., Massachusetts Institute of Technology, Cambridge, Mass.
25. Sahoo, P., Collur, M. M., and DebRoy, T. 1988. Effects of oxygen and sulfur on alloying element vaporization rates during laser welding. *Metallurgical Transactions B-Process Metallurgy* 19(6): 967-972.
26. Adonyi, Y., Richardson, R. W., and Baseslack III, W. A. 1992. Investigation of arc effects in subsurface GTA welding. *Welding Journal* 71(9): 321-s to 330-s.
27. Lin, M. L. 1985. Transport process affecting the shape of arc welds. Ph.D. diss., Massachusetts Institute of Technology, Cambridge, Mass.
28. Tsai, N.-S. 1983. Heat distribution and weld bead geometry in arc welding. Ph.D. diss., Massachusetts Institute of Technology, Cambridge, Mass.
29. Kokura, S., Nihei, M., Kozono, U., Ashida, E., and Onuma, A. 1980. Studies on twin electrode switching arc welding method (Report 1) — High speed welding with twin electrode switching TIG. *Quarterly Journal of the Japan Welding Society* 49(4): 259-265.
30. Chihoski, R. A. 1968. The effects of varying electrode shapes on arc, operations, and quality of welds in 2014-T6 aluminum. *Welding Journal* 47(5): 210-s to 222-s.
31. Lee, S.-Y., and Na, S.-J. 1996. A numerical analysis of a stationary gas tungsten arc considering various electrode angles. *Welding Journal* 75(9): 269-s to 279-s.
32. Grigorenko, V. V., Kiselev, O. N., Chernyshov, G. G., Gladkov, E. A., Rybachuk, A. M., Bobylev, Y. N., Zhulidov, N. V., and Poklonov, G. G. 1997. Formation of defect-free welded joints at higher speeds in automatic argon TIG welding thin-wall pipes. *Welding International* 11(1): 58-60.